Precision Engineering 100 (2026) 1–12

Contents lists available at ScienceDirect

Precision Engineering

journal homepage: www.elsevier.com/locate/precision

Fundamental investigation of femtosecond pulsed laser micromachining mechanisms for single-crystal diamond

Kodai Koshiishi, Yuka Yamamuro, Jiwang Yan *

Department of Mechanical Engineering, Faculty of Science and Technology, Keio University, Hiyoshi 3-14-1, Kohoku-ku, Yokohama, 223-8522, Japan

A R T I C L E I N F O

Keywords:
Single-crystal diamond
Femtosecond pulsed laser
LIPSS
Graphitization
Surface roughness
Raman spectroscopy
Micro cavity

A B S T R A C T

Single-crystal diamond (SCD) has excellent mechanical, thermal and physical properties that rank among the highest of all substances. It has widespread applications in diverse fields such as cutting tools, optical windows, spintronics and power electronics. However, SCD is difficult to machine via mechanical processes due to its extremely high hardness. In recent years, laser processing has attracted attention since it enables non-contact efficient machining regardless of material hardness. In this study, femtosecond pulsed laser, which is considered to be capable of high-precision machining with low thermal effect, was used for micromachining of SCD, and the effects of laser irradiation parameters on the surface texture, roughness and profile geometry, as well as subsurface material structural changes, were investigated. It was found that even under femtosecond pulses thermal effect existed and that using a higher laser scanning speed was helpful to eliminate thermal cracks formation. The laser machined surfaces were covered with nanoscale periodical surface ripples with a surface roughness in the level of 0.10 μm Ra. Raman analysis of the SCD surface after laser machining showed that amorphous carbon and nanocrystalline graphite existed as a composite material. The graphitization depended on the laser fluence and hatching width and was particularly pronounced at low fluence and small hatching width. It was also demonstrated that acid cleaning could remove most of the graphite layer and reduce surface roughness. As samples, a few three-dimensional micro cavities with flat bottoms and sharp corners were created. This study demonstrates that femtosecond pulsed laser is a suitable method for machining micro three-dimensional shapes in SCD while it is important to optimize the laser machining conditions to avoid thermal damage and improve the surface quality.

1. Introduction

Single-crystal diamond (SCD) has excellent mechanical and thermal physical properties, such as high hardness, high thermal conductivity, low thermal expansion, and wear resistance. Thanks to these unique material properties, it is used in a wide range of fields such as ultra-precision cutting tools [1], optical components [2], power electronic devices [3], and micro-electromechanical systems (MEMS) [4]. The demand for precision machining technology of SCD microscale arbitrary shapes is expected to increase extensively in the future. Conventionally, SCD is machined by lapping or polishing using fine diamond abrasives. However, these abrasive processes are difficult to machine SCD into the desired micro three-dimensional shapes. Although reactive ion etching (RIE) is suitable for fabricating such shapes, a number of process steps, including mask coating, are necessary, and the total processing time is very long [5].

In comparison, laser micromachining, which enables non-contact local microfabrication of arbitrary three-dimensional shapes, is attracting attention as one of the effective methods with high efficiency [6,7]. By scanning a laser beam, it is possible to create various micro complex shapes in a short time, regardless of material hardness. For laser micromachining, Odake et al. [8] showed that irradiating SCD with a nanosecond pulsed laser created a thick graphite layer. The layer was significantly distorted and could damage the underlying diamond layer. Takayama et al. [9] machined microgrooves by irradiating a nanosecond pulsed laser on SCD surfaces. They reported that the irradiated areas turned into graphite because of the thermal effect and observed micro-crack generation on the groove walls. By using a picosecond pulsed laser, thermal cracking was suppressed and graphitization became less significant [10]. Okamoto et al. [11] performed laser microgrooving of

This article is part of a special issue entitled: JSPE selected papers published in Precision Engineering.

* Corresponding author.
E-mail address: yan@mech.keio.ac.jp (J. Yan).

https://doi.org/10.1016/j.precisioneng.2026.02.015
Received 21 December 2025; Received in revised form 6 February 2026; Accepted 24 February 2026
Available online 25 February 2026

SCD by irradiating a nanosecond pulsed laser and confirmed that graphitization was very significant, but the bottom surface of the grooves was flattened after removing the graphitized area by acid cleaning. However, the laser beam needed to irradiate each spot with approximately 5000 shots at a pulse repetition frequency of 50 kHz to obtain a deep groove due to the existence of the thick graphite layer caused by the nanosecond pulsed laser irradiation. This leads to a long processing time per unit area. From the above-mentioned previous studies, it is known that nanosecond pulsed laser processing causes severe graphitization of SCD and surface thermal cracking. Furthermore, it is difficult to achieve high-precision shape creation and high-quality surface finishing.

Femtosecond pulsed lasers have attracted particular attention in recent years. Unlike lasers with longer pulses, such as nanosecond pulses, the femtosecond pulsed laser process can remove a small volume of material before heat conduction occurs, resulting in less heat affected zone (HAZ) [12]. Wang et al. [13] reported that by using a femtosecond pulsed laser, graphitization of SCD was less likely to occur than using a nanosecond pulsed laser, and Wu et al. [14] achieved making dimples on SCD without generating microcracks by using a femtosecond pulsed laser.

However, the material removal mechanisms of SCD under femtosecond pulses remain unclear and there is little literature on femtosecond pulsed laser microfabrication of three-dimensional SCD structures by considering the processing characteristics resulting from the interaction between the laser beam and the SCD material. For example, Granados et al. [15] processed SCD with hatching irradiation over a wide surface area and observed the changes in the surface structure. However, they did not examine the entire surface in terms of depth change. Banik et al. [16] performed hatching irradiation of a femtosecond pulsed laser onto a flat SCD surface and investigated the features of the laser irradiated surface and found that the characteristic surface structure was laser-induced periodic surface structures (LIPSS). However, the appropriate laser scanning interval for obtaining a flat surface has not been investigated, and the change in surface depth by repeated irradiation has not been clarified. Furthermore, to date, no research has been conducted on the changes in the material removal mechanisms, including diamond graphitization, when the hatching width is changed in creating a three-dimensional shape.

The objective of this study was to achieve high-precision microfabrication of SCD using a femtosecond pulsed laser for three-dimensional shapes with high surface quality and low subsurface damage. The effects of laser irradiation parameters on the processing characteristics of SCD were investigated by evaluating the surface morphology, profile depth, surface roughness, and changes in material structure before and after acid cleaning. By clarifying the mechanism of the interaction between femtosecond pulses and SCD, the fabrication of rectangular micro cavities with flat bottom surfaces and sharp corners was demonstrated and the resulting surface quality and shape accuracy were evaluated.

2. Materials and methods

2.1. Materials

An SCD substrate produced by chemical vapor deposition (CVD) was used as a sample. The sample was prepared as a rectangular plate with dimensions of 3.5 mm × 4.0 mm × 1.1 mm. The surface was mirror-polished and had a surface roughness of 0.31 ± 0.08 μm Ra. All six surfaces of the sample were equivalent to (100) Miller crystalline planes. Before laser irradiation experiment, the sample was cleaned with ethanol and then air-dried.

2.2. Laser irradiation setup and conditions

The laser system used in this study is schematically shown in Fig. 1 (a), which consists of a laser oscillator, beam expander, attenuator, polarizer, galvanometer scanner, Fθ lens, and stage. Fig. 1(b) shows a photograph of the processing section of the setup where the positions of the sample, the stage, the Fθ lens, and the vacuum cleaner are indicated. The laser source used was a linearly polarized femtosecond Yb: KGW laser (PHAROS-08-600-PP, Light Conversion, UAB, Lithuania), which produced a laser beam with a Gaussian energy distribution at a wavelength of 1028 nm with 256 fs pulse width. The beam has linear polarization direction. The laser parameters are summarized in Table 1. The Fθ lens, whose focal length is 70 mm, was used to focus the collimated laser beam into a spot 16 μm in diameter. The laser beam was

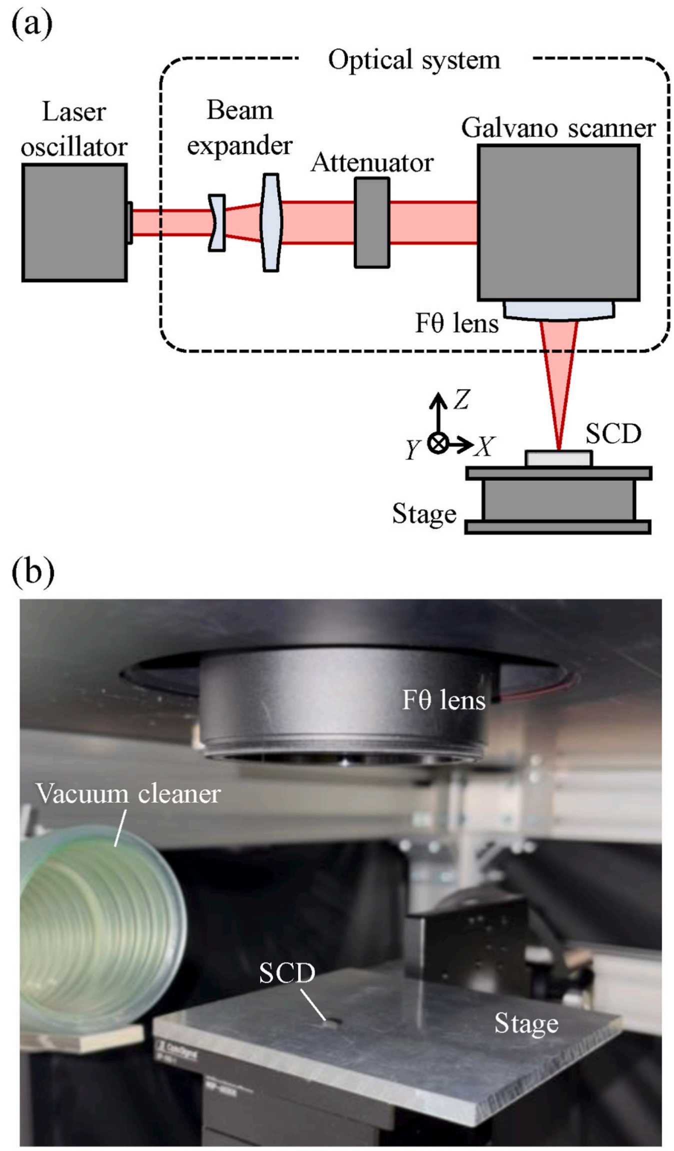

Fig. 1. (a) Schematic of experimental setup for femtosecond pulsed laser irradiation, (b) photograph of the processing section of the setup.

Table 1
Laser parameters.

Laser medium	Yb: KGW
Laser wavelength [nm]	1028
Spot diameter [μm]	16
Pulse width [fs]	256
Repetition frequency [kHz]	100
Beam energy distribution	Gaussian
Irradiation atmosphere	Air

scanned in X and Y directions on the sample by controlling a galvanometer scanning system, and the distance between the laser focal point and the sample surface was adjusted by a manual stage in the Z direction. Laser wavelength, spot diameter, pulse width, and repetition frequency were kept constant for all experiments.

The experimental conditions are shown in Table 2, and the irradiation schemes in Fig. 2. First, to investigate the fundamental microgrooving characteristics of SCD, line irradiation experiments were conducted by varying the laser scanning speed, laser fluence, and the number of scans. Laser fluence was set at two levels, 2.0 J/cm^2 and 3.5 J/cm^2, respectively. The laser beam was repeatedly scanned over the same location, as shown in Fig. 2(a). Next, to evaluate surface roughness and topography over a larger area for three-dimensional micromachining, hatching irradiation experiments were conducted. As shown in Fig. 2(b), the laser beam was raster scanned in both directions at regular intervals and repeated multiple times at the same region. The scanning speed and number of scans were kept constant, while the laser fluence and hatching width were varied. During the irradiation process, the debris was sucked up by a vacuum cleaner.

2.3. Measurement and characterization methods

After laser irradiation, the cross-sectional profiles and surface roughness of SCDs were measured using an optical microscope (VK-X1000, Keyence Corp., Japan). In hatching irradiation experiments, the surface roughness evaluation areas were selected within the central 100 μm × 100 μm region of the irradiation area. Measurement direction is perpendicular to the irradiation direction, same as the measurement direction in Fig. 2(b), using a × 50 objective lens. The objective lens resolution is 5 nm in the height direction, which is sufficiently small relative to the surface topography scale. The measurement length was approximately 100 μm, with the roughness cut-off length of 80 μm. This setting is sufficiently large relative to both nanoscale LIPSS structures and micro undulations made by hatching irradiation. Therefore, the surface roughness quantifies the combined effect of LIPSS-induced micro-texture and the undulations associated with the hatching pattern. The error bars represent the standard deviation of measurements taken at eleven different locations. A field-emission scanning electron microscope (FE-SEM, JSM-IT700HR/LA, JEOL Ltd., Japan) was used to observe the surface morphology of the sample. For the SEM observations, the sample was coated with osmium to improve electrical conductivity. A laser micro-Raman spectrometer (InVia Raman Microscope, Renishaw plc., UK) was used to evaluate the crystallinity of the sample surface before and after laser irradiation.

To investigate the graphitization of the surface that occurred during laser processing of SCD and its effect on surface roughness and topography, acid cleaning of the sample was performed to remove the graphitized layer to expose the bulk of the substrate. A mixture of 3 mL perchloric acid (70 wt%), 5 mL sulfuric acid (95 wt%), and 1 mL nitric acid (70 wt%) was prepared and heated to 200 °C [17–19]. The sample was immersed in the solution for 30 min and then cleaned with large volumes of distilled water.

Table 2
Experimental conditions.

	(a) Line irradiation	(b) Hatching irradiation
Scanning speed: V [mm/s]	10, 50, 100	50
Energy density: E [J/cm^2]	2.0, 3.5	2.0, 3.5
Number of scans: N	1 ~ 20	5
Hatching width [μm]	-	2.0 ~ 16.0

3. Results and discussion

3.1. Microgrooving by line irradiation

To investigate the fundamental microgrooving characteristics of SCD, line irradiation experiments were conducted. Fig. 3 shows SEM images of the SCD surface irradiated at different scanning speeds and numbers of scans. The laser fluence used was 2.0 and 3.5 J/cm^2. At both fluences, LIPSS were uniformly formed on the entire surface, and oriented perpendicular to the linear polarization. The polarization direction was perpendicular to the laser scanning direction, resulting in LIPSS being formed parallel to the laser scanning direction. At a scanning speed of 10 mm/s, many microcracks were observed both inside and outside the groove when $N \geqq 1$, and severe debris deposition was observed around the irradiated area at $N \geqq 10$. All cracks outside the groove in Fig. 3(b) formed at a 45° angle, which are thought to be due to crack propagation along the (111) plane. These cracks extend slightly from outside the groove to the inner groove wall, and all are considered to be cracks on the same plane. The cracks inside the groove in Fig. 3(a) also show the same orientation as the inner wall portion of the cracks in Fig. 3(b), suggesting they are also on the (111) plane. On the other hand, no microcracks were generated at 50 and 100 mm/s. From these results, it is presumable that thermal effects cannot be completely ignored even for femtosecond pulses. In this experiment, the occurrence of cracks differed depending on the scanning speed. To discuss the result, the relationship between femtosecond pulsed laser irradiation and the change in surface temperatures is considered. The discussion is simplified based on scanning speed. Taylor et al. [20] reported that for silicon targets, the sample surface temperature increased stepwise under the influence of successive irradiation pulses, and the attained temperature depended on the scanning speed. The lower scanning speeds resulted in greater temperature rise on the irradiated surface. The sample material is different in this study, however, it is considered that a similar argument can be applied to single-crystal diamond. According to the results in the figures, cracks formed at scanning speed of 10 mm/s, on the other hand, crack generation was suppressed by increasing the speed to 50 mm/s. The pulse overlap rate at 10 mm/s and 50 mm/s are 99.4% and 96.9%, respectively. Thus, it is clear that the cracks generation threshold at laser fluence of 2.0 J/cm^2 and $N = 1$ exists within this range of pulse overlap rate. It is assumed that lower scanning speeds also caused a greater accumulation of heat at the irradiated surface. Furthermore, as later results indicate, graphitization occurred in the irradiated area, making surface temperature increase more likely. Cracks formed due to a combination of factors, including a slight increase in volume and changes in the thermal parameters. Thus, for high-precision processing of SCD, it is needed to select an appropriate laser scanning speed. In this study, 50 mm/s was used for the following experiment.

Fig. 4 shows the change in groove depth after irradiation at a laser fluence of 2.0 J/cm^2. The groove's depth increased as the scanning speed decreased. This is because the increase in laser energy input per unit area due to the increased pulse overlap rate as the scanning speed decreased, resulting in more material removal. Fig. 5 shows the cross-sectional profiles of the groove after acid cleaning irradiated at a laser fluence of 3.5 J/cm^2 and the scanning speed of 50 mm/s, and various numbers of scans. Again, it is confirmed that the groove depth increases as the number of scans increases. This is due to the increase in energy to the same area as the number of scans increased, and the amount of material removed increased accordingly. The change in groove shape with increasing number of scans shows that, around $N = 5$, the groove gradually shifts from a U-shape to a sharper profile, approaching a V-shape. In addition, since the profile change is greater in the center of the groove compared to its sides, it can be explained that material removal due to ablation is greater near the groove center than at the sides. As the number of scans increases, the surface area inside the groove increases. The mechanism of the groove shape changing from U-shape to V-shape is considered to be the same as the mechanism for the V-groove shape

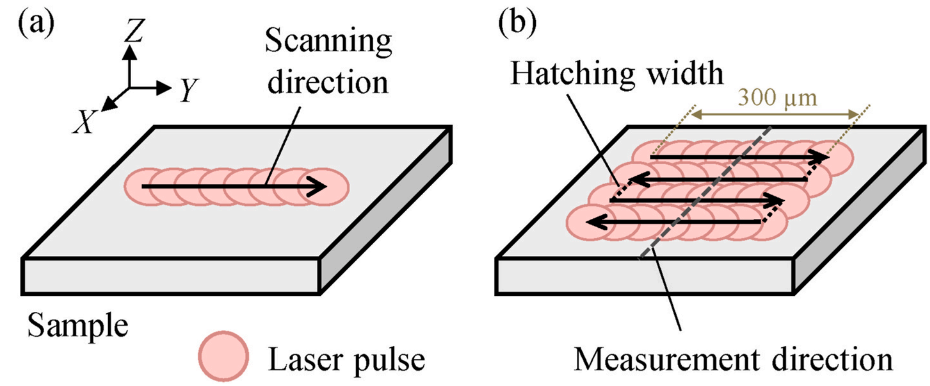

Fig. 2. Laser irradiation schemes: (a) line irradiation, and (b) hatching irradiation.

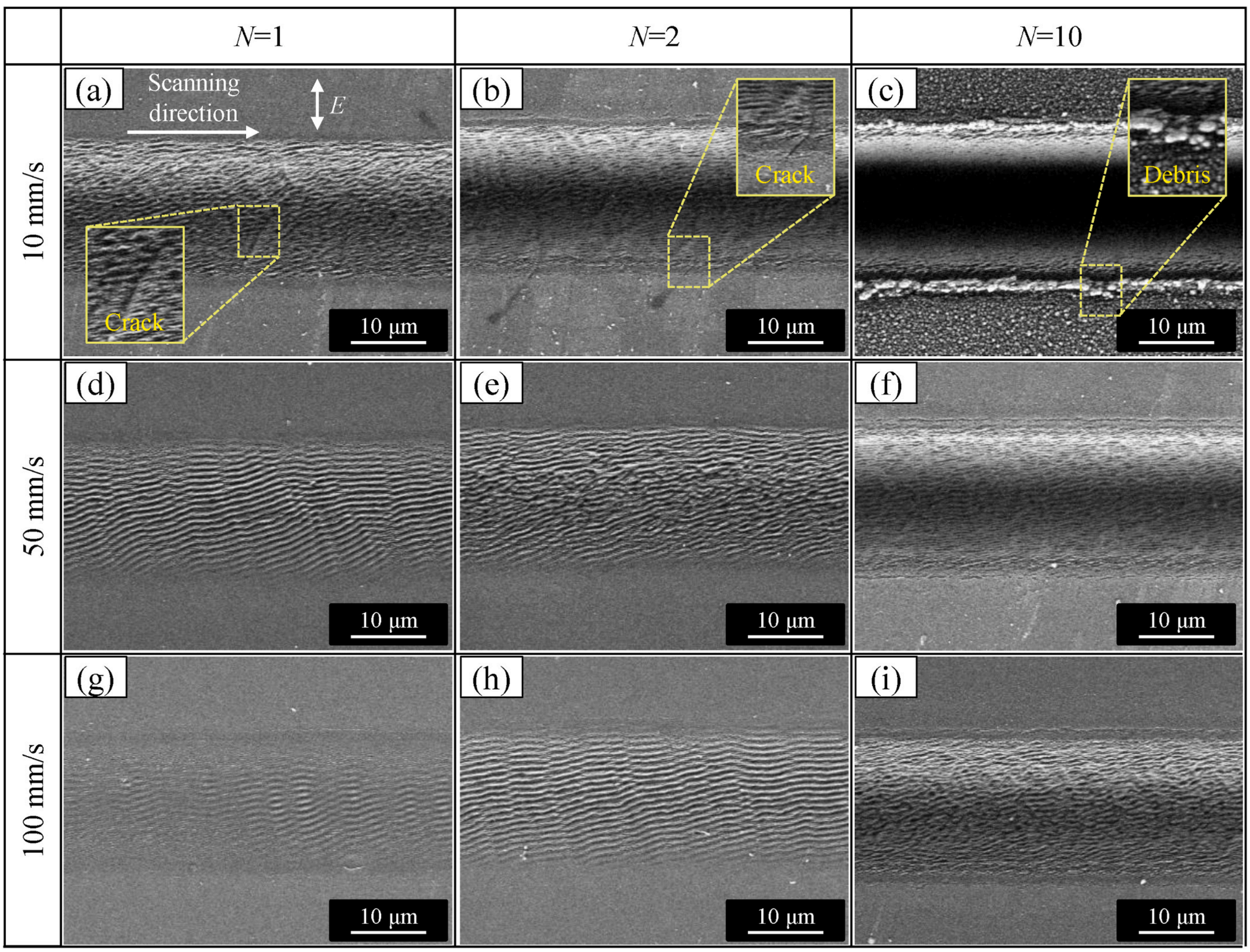

Fig. 3. SEM images of the groove surface after laser irradiation at laser fluence of 2.0 J/cm^2, at different scanning speeds and numbers of scans.

formed during laser irradiation of zirconia observed by Yamamuro et al. [21]. At the groove walls, the angle between the wall and the laser beam axis becomes larger, increasing the cross-sectional area exposed to the laser beam. Consequently, the actual fluence decreases, reducing the material removal rate at the walls. In contrast, closer to the groove center, the cross-sectional area does not change as significantly as at the walls. Fluence decreases less, and material removal progresses. Due to these mechanisms, the groove shape transitions from U-shape to V-shape. The 16 μm spot diameter used in this study is defined at the position where the intensity reaches 1/e^2 of its peak value, and non-negligible energy also exists outside this diameter. Even outside the defined spot diameter, sufficient light intensity remains to cause multiphoton absorption, suggesting that material removal occurred. As a result, material removal near the surface reached nearly twice the spot diameter. However, most of the machining occurs within the 16 μm range defined by the spot diameter, which corresponds well to the

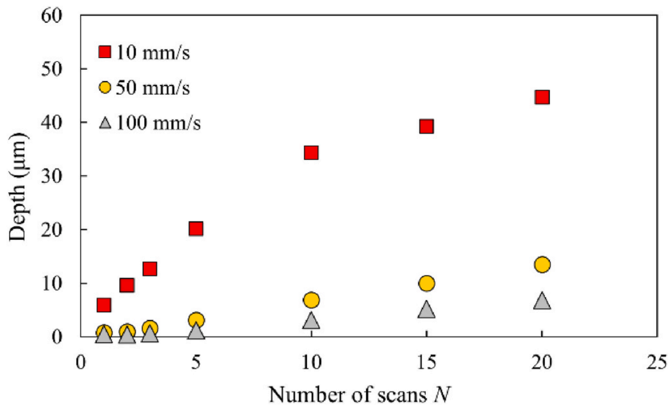

Fig. 4. Change in groove depth with different numbers of scans irradiated at laser fluence of 2.0 J/cm^2, at scanning speeds of 10, 50, and 100 mm/s.

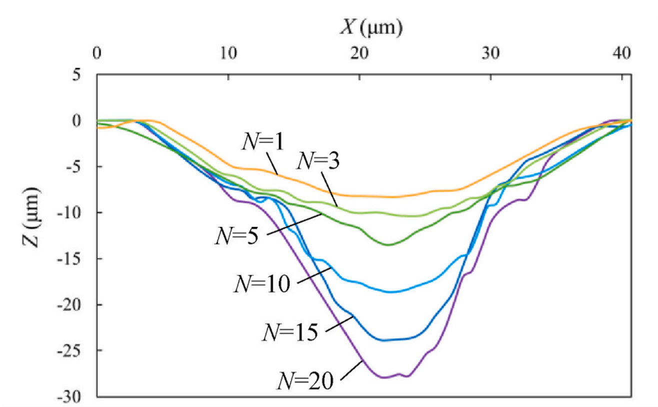

Fig. 5. Cross-sectional profiles of microgroove after acid cleaning irradiated at laser fluence of 3.5 J/cm^2, at different numbers of scans.

V-shape area. Based on this profile measurement, selecting a value around $N = 5$, which efficiently removes material while preventing the groove wall slope from becoming excessively sharp, is thought to result in a flat surface during hatching irradiation.

3.2. Surface flattening by hatching irradiation

To investigate the irradiation characteristics for fabricating flat surfaces, hatching irradiation was conducted. Based on the aforementioned experimental results, the irradiation parameters of scanning speed and number of scans were determined as shown in Table 2(b). The LIPSS periods fabricated by several laser parameters used in the hatching irradiation experiment were measured, as listed in Table 3. The results revealed that the period of the LIPSS was approximately 0.83 μm and there were no significant changes within irradiation parameters, such as hatching width and laser power, which varied in this experiment. In general, the LIPSS period is highly dependent on the laser wavelength; in other words, within the parameter ranges used in this experiment, no significant difference appeared in the LIPSS period. This study primarily targets shape processing at scales ranging from submillimeter to several hundred micrometers. The discussion on how LIPSS relates to surface roughness is covered in a later chapter. In this study, the LIPSS period remained almost unchanged with parameter variations, so parameter comparisons have been simplified, and the discussion on LIPSS is limited to this extent. Fig. 6 shows the SEM images of the SCD surfaces fabricated by the hatching irradiation at a laser fluence of 2.0 J/cm^2. The SEM observation was performed after acid cleaning. For the hatching width of 3 μm, microcracks were observed on the surface (Fig. 6(a)). During line irradiation at 50 mm/s, no cracks were observed. However, during hatching irradiation, microcracks were partially observed. Smaller hatching widths resulted in overlapping scan lines, leading to different processing characteristics compared to simple line irradiation. Changes in surface thermal properties due to the scan line overlap caused crack formation due to thermal stress. Note that detailed discussions on the effects of each parameter regarding graphitization of the laser-irradiated surface in this study are presented in Chapter 3.3 and subsequent sections. At bigger hatching widths, no cracks were found (Fig. 6(b) and (c)). The cracks are similar to those identified on the edges of the microgrooves during line irradiation (Fig. 3) and are thought to be caused by thermal accumulation. For the magnified images, it was found that LIPSS partially formed non-uniformly, and some of them collapsed when hatching widths were small, as shown in Fig. 6(d) and (e). On the other hand, for the larger hatching width, LIPSS formed uniformly over the entire surface as shown in Fig. 6(f).

Table 3
LIPSS periods at different laser fluence and hatching widths after acid cleaning.

Fluence [J/cm^2]	Hatching width [μm]	LIPSS period [μm]
2.0	9	0.83 ± 0.01
	12	0.83 ± 0.02
3.5	4	0.82 ± 0.01
	6	0.82 ± 0.01
	9	0.83 ± 0.01
	12	0.83 ± 0.01

To investigate the effect of acid cleaning, SEM image of the irradiated surface before acid cleaning with the hatching width of 3 μm is shown in Fig. 7. The surface is covered with LIPSS, and there was no damaged non-uniform LIPSS. According to Figs. 6 and 7, it is considered that the laser-induced graphitized layer on LIPSS, which were uniform, was removed by the acid cleaning, resulting in a non-uniform LIPSS. The reason for the non-uniformity is that even if LIPSS appear uniformly formed visually before acid cleaning, its structure consists mostly of graphite. Only some areas where LIPSS were directly imparted onto the diamond structure remain as LIPSS, while the rest is removed. It was found that the smaller the hatching width, the more the LIPSS, which were made of graphite, were removed.

Fig. 8 shows the SEM images of the SCD surfaces machined at a laser fluence of 3.5 J/cm^2 after acid cleaning. For the hatching width of 9 μm, a smooth surface consisting of uniform LIPSS without any cracks was observed. By increasing the hatching width, micro-scale periodic uneven surfaces were generated corresponding to the hatching width of the laser beam scan. Fig. 9 shows the cross-sectional profile of Fig. 8(c). At every 16 μm, which is the same as the hatching width, a concave area was observed where the laser beam had scanned. The amount of material removal for laser scan corresponded to the Gaussian energy distribution of the laser beam; therefore, as the hatching width approaches 16 μm, which is the laser spot diameter, the removal shape at the laser irradiation position became more pronounced, and the periodic U-shaped concave-convex pattern became increasingly prominent.

Fig. 10 shows the relationship between the hatching width and surface roughness. The surface patterns formed by hatching irradiation (Figs. 8 and 9) and LIPSS (Figs. 6–8) were oriented in the same direction. Therefore, Ra was used to simultaneously assess both effects. This enabled direct examination of the surface profile formed by hatch irradiation. Before acid cleaning (Fig. 10 (a)), the smallest surface roughness was obtained when the hatching width was between 5 and 8 μm for both energy densities. The surface roughness at this point was approximately 0.10 μm Ra. For hatching widths larger than 9 μm, the surface roughness tended to increase as the hatching width increased, and surface roughness was larger at 3.5 J/cm^2 than at 2.0 J/cm^2.

After acid cleaning (Fig. 10(b)), surface roughness was almost constant between 2 and 12 μm hatching width. The minimum value was below 0.10 μm Ra at a hatching width of 9 μm. The acid cleaning

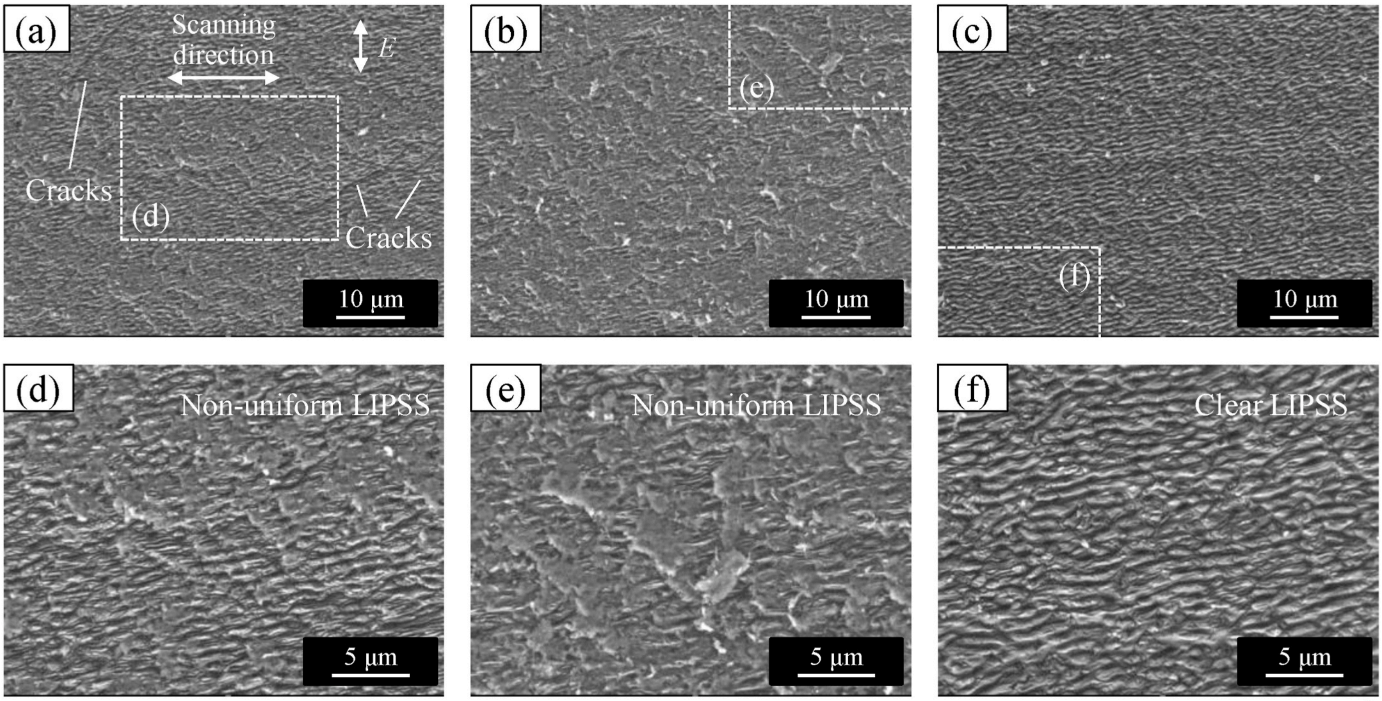

Fig. 6. SEM images of the irradiated surfaces after acid cleaning at laser fluence of 2.0 J/cm^2, at different hatching widths: (a) 3 μm, (b) 5 μm, (c) 9 μm. (d), (e), and (f) are enlarged versions of (a), (b), and (c), respectively, at twice the size.

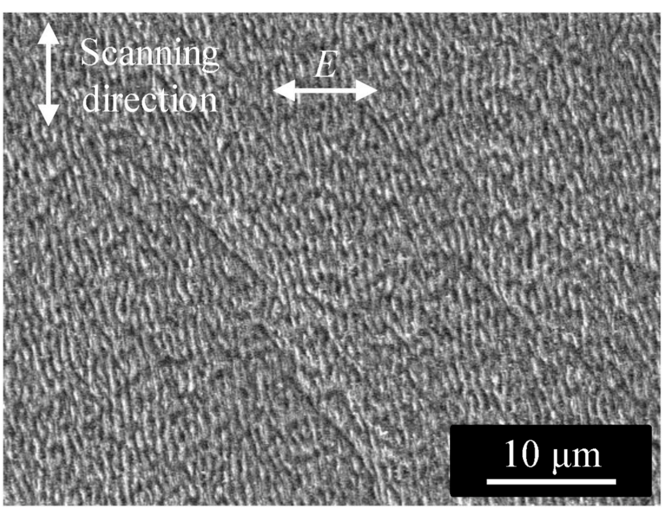

Fig. 7. SEM image of irradiated surface before acid cleaning at laser fluence of 2.0 J/cm^2, at hatching width of 3 μm.

removes the non-diamond structure from the surface of the specimen, especially at hatching widths of 2 to 4 μm, and the removal of the graphitized part of the surface shows a marked difference to that before the acid cleaning. The reduction in surface roughness in other hatching

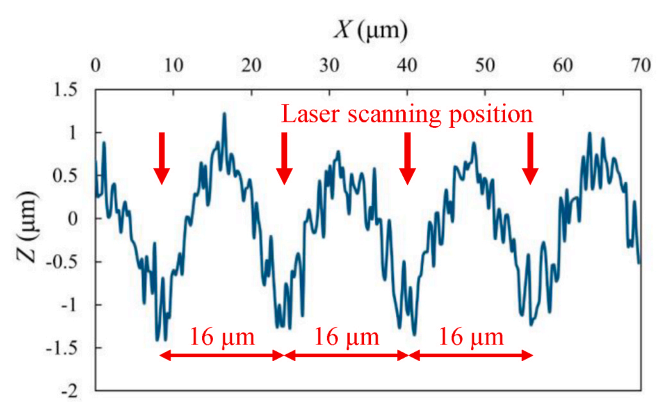

Fig. 9. Enlarged cross-sectional profile of Fig. 8(c).

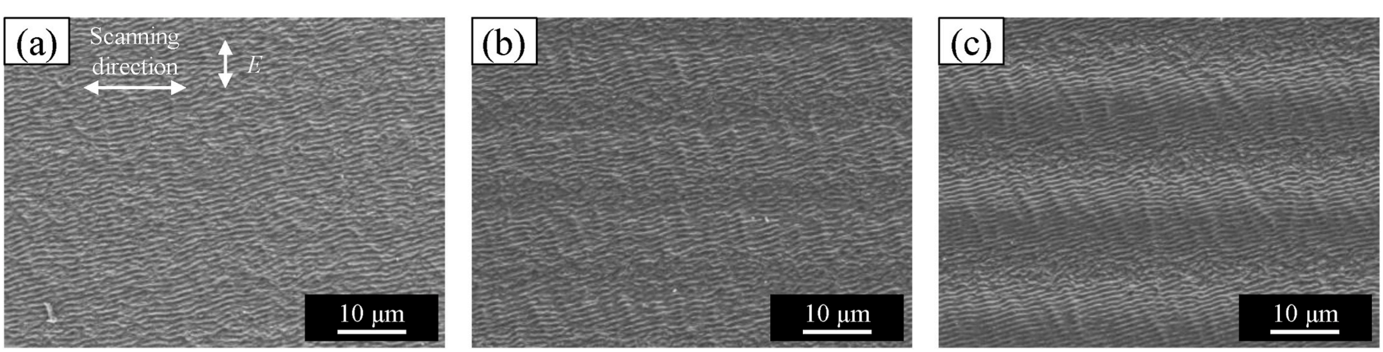

Fig. 8. SEM images of irradiated surface after acid cleaning at laser fluence of 3.5 J/cm^2, at different hatching widths: (a) 9 μm, (b) 12 μm, (c) 16 μm.

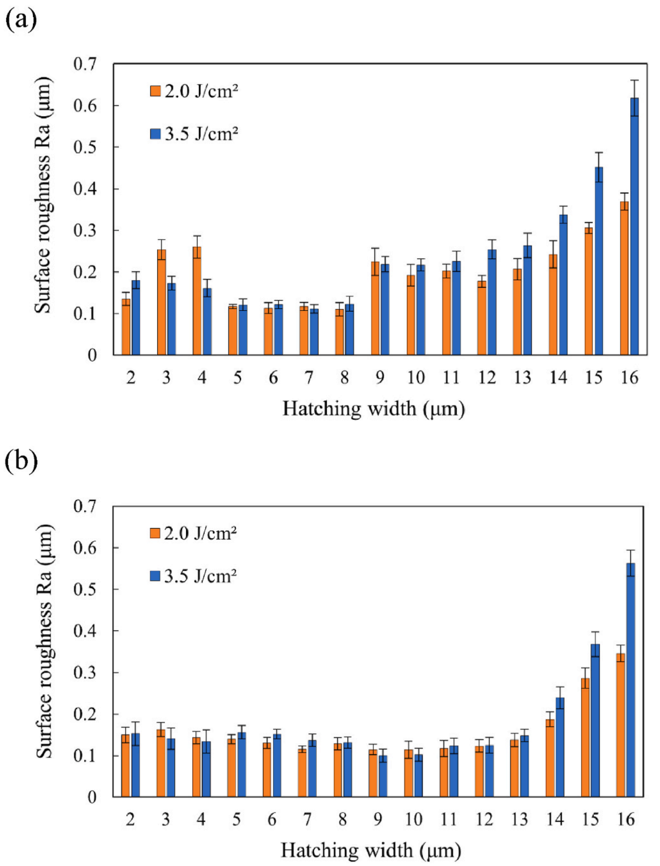

Fig. 10. Change in surface roughness with various hatching widths (a) before and (b) after acid cleaning.

widths may be due to the removal of surface structures that have been transformed other than diamonds. From the comparison of surface roughness in Fig. 10(a) and (b), the thickness of the graphite layer removed by acid cleaning is estimated to be from several tens of nanometers to approximately 100 nm. The increase in the influence of the laser energy distribution with increasing hatching width was also observed after acid cleaning. The period of the LIPSS was about 0.83 μm, but the depth can be estimated to be much smaller than the period, suggesting that the LIPSS generated on the surface determined a minimum surface roughness of approximately 0.10 μm Ra. Furthermore, the difference in surface roughness between 2.0 J/cm^2 and 3.5 J/cm^2 became smaller when the hatching width was 9 μm or bigger. However, when the hatching width was large (14 μm to 16 μm), the surface roughness at 3.5 J/cm^2 was still larger than that at 2.0 J/cm^2.

3.3. Raman analysis of machined surfaces

To evaluate the crystallinity of the SCD surface after laser irradiation, Raman analysis was conducted. Fig. 11 shows the Raman spectra of the unirradiated surface and laser irradiated surface at different laser fluence and hatching widths, both before and after acid cleaning. In general, the peak around 1332 cm^{-1} is derived from the diamond crystal, the peak around 1425 cm^{-1} is from nitrogen-vacancy (NV) [22], and the peak around 1580 cm^{-1} (G peak) is from graphite structures, and the 1350 cm^{-1} peak (D peak) is from defects in the graphite structure [23,24]. The graphite structure generated by laser irradiation is a composite material in which amorphous carbon, which is highly amorphous, and nanocrystalline graphite, which is highly crystalline and has a grain size of several tens of nm, exist simultaneously as a gradation [25,26]. Therefore, the G peak represents the structure of nanocrystalline diamond and the presence of amorphous carbon, while the D peak represents defects in the amorphous structure and nanocrystalline graphite.

In both figures of Fig. 11, peaks derived from diamond crystals and NV were seen in all conditions, while the D peak did not clearly appear. On the other hand, in both Fig. 11(a) and (b), the G peak was more pronounced when the hatching width was 2 and 5 μm before acid cleaning. As the hatching width increased to 8 μm, the G peak was present but not pronounced. This indicates that when the hatching width is smaller than the laser spot diameter, the crystal structure of the irradiated surface changes due to laser irradiation, and graphitization is likely to occur. The G peak at a hatching width of 2 μm is larger at a lower fluence of 2.0 J/cm^2 than at a higher fluence of 3.5 J/cm^2, indicating that graphitization is particularly likely to occur at low fluences and small hatching widths. The Raman spectra after acid cleaning show that the clear G peak disappears in all conditions and is significantly reduced at a hatching width of 2 μm and 5 μm, where the G peak was particularly prominent, indicating that the acid cleaning removes the graphite-structured portions.

Fig. 12 shows the Raman spectra of the irradiated surface at laser fluence of 2.0 J/cm^2 before and after acid cleaning, at hatching width of 2 μm. For the peak analysis, the spectra were fitted with a Gaussian curve with the aforementioned four peaks (Diamond, NV, G, and D peaks). This figure clearly shows that the G peak, which was prominent before the acid cleaning in Fig. 12(a), is greatly reduced after the acid cleaning in Fig. 12(b). However, not all the G peaks disappeared, suggesting that a small amount of graphite structure remains even after acid cleaning. In addition, the D peak, which could not be clearly identified in Fig. 11, can be seen by peak separation, suggesting that the graphite structure generated by laser irradiation is amorphous or crystalline structure with defects.

Fig. 13 shows I_D/I_G, $I_G/I_{Diamond}$, and $I_D/I_{Diamond}$ ratio of the laser irradiated surface at different laser fluence and hatching widths. I_D, I_G, and $I_{Diamond}$ represent the integrated intensity of D peak, G peak, diamond crystal peak, respectively. I_D/I_G indicates the proportion of defects in the graphite structure relative to the entire graphite structure. $I_G/I_{Diamond}$ indicates the proportion of the entire graphite structure relative to the diamond structure, and this value indicates the amount of graphite structure relative to diamond. $I_D/I_{Diamond}$ indicates the proportion of defects in the graphite structure relative to the entire diamond structure, and this value indicates the amount of amorphous carbon or defective part of nanocrystalline graphite relative to the diamond structure. By comparing the ratios, differences in hatching width and fluence, as well as laser-induced changes in graphite structure due to acid cleaning, can be analyzed in detail. First, the machined samples before acid cleaning were compared. From Fig. 13(a), (b), and (c), when the laser fluence is 2.0 J/cm^2, I_D/I_G increases, and $I_G/I_{Diamond}$ and $I_D/I_{Diamond}$ decrease as the hatching width increases. The increase in I_D/I_G indicates that the proportion of amorphous carbon has increased. $I_G/I_{Diamond}$ and $I_D/I_{Diamond}$ are decreasing, indicating that the larger the hatching width, the graphitization is suppressed, and the total amount of graphite layer produced is decreasing. Fig. 13(d), (e), and (f) show that I_D/I_G tended to increase with increasing hatching width at fluence 3.5 J/cm^2, but $I_G/I_{Diamond}$ and $I_D/I_{Diamond}$ were both maximum at a hatching width of 5 μm. Therefore, it is considered that ablation-based material removal was dominant without significant diamond amorphization occurring when the hatching width was 2 μm due to the larger overlap of line irradiations.

Next, the machined samples after acid cleaning were compared. From Fig. 13(a), (b), and (c), I_D/I_G increased significantly at all hatching widths compared to that before acid cleaning when the fluence was 2.0 J/cm^2. Also, $I_G/I_{Diamond}$ decreased significantly at all hatching widths. This indicates that the acid cleaning significantly removes the graphite structure, and the smaller the hatching width, the more graphite structure remains after the acid cleaning. The remaining graphite structure is limited to the stable structure at the interface between the graphite and diamond layers [27,28]. The $I_D/I_{Diamond}$ tended to decrease compared to

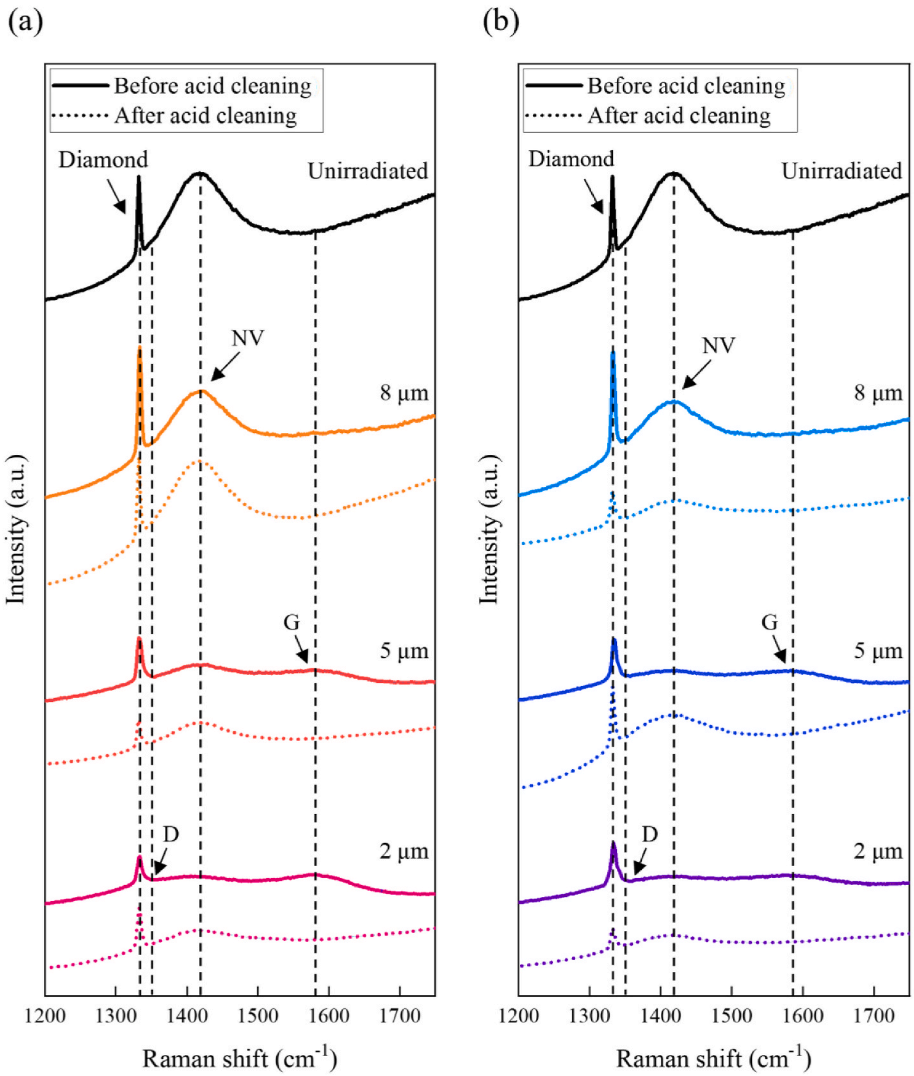

Fig. 11. Raman spectra of the unirradiated and laser irradiated surface at laser fluence of (a) 2.0 J/cm^2 and (b) 3.5 J/cm^2, both before and after acid cleaning at different hatching widths.

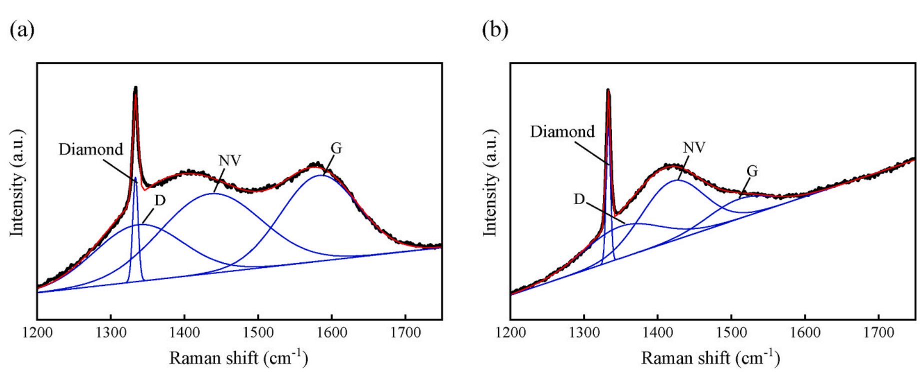

Fig. 12. Raman spectra of the laser irradiated surface at laser fluence of 2.0 J/cm^2 at hatching width of 2.0 µm, (a) before and (b) after acid cleaning. Decomposed four peaks and the baseline are displayed in blue, and their sum is shown in red. Four components: in the order of (a) to (b), Diamond bands at both 1333 cm^{-1}, D bands at 1337 and 1350 cm^{-1}, NV bands at 1435 and 1420 cm^{-1}, G bands at 1583 and 1511 cm^{-1}. (For interpretation of the references to colour in this figure legend, the reader is referred to the Web version of this article.)

that before acid cleaning, but increased at a hatching width of 8 µm. This suggests that defects in the structure of the nanocrystalline graphite that could not be removed increased compared to those before the acid cleaning. Fig. 13(e) shows that the $I_G/I_{Diamond}$ decreased significantly at all hatching widths, confirming that the acid cleaning significantly removed the entire amorphous graphite and most of the nanocrystalline graphite when the fluence was 3.5 J/cm^2, as same as 2.0 J/cm^2. From Fig. 13(f), it was confirmed that defects in the remaining nanocrystalline

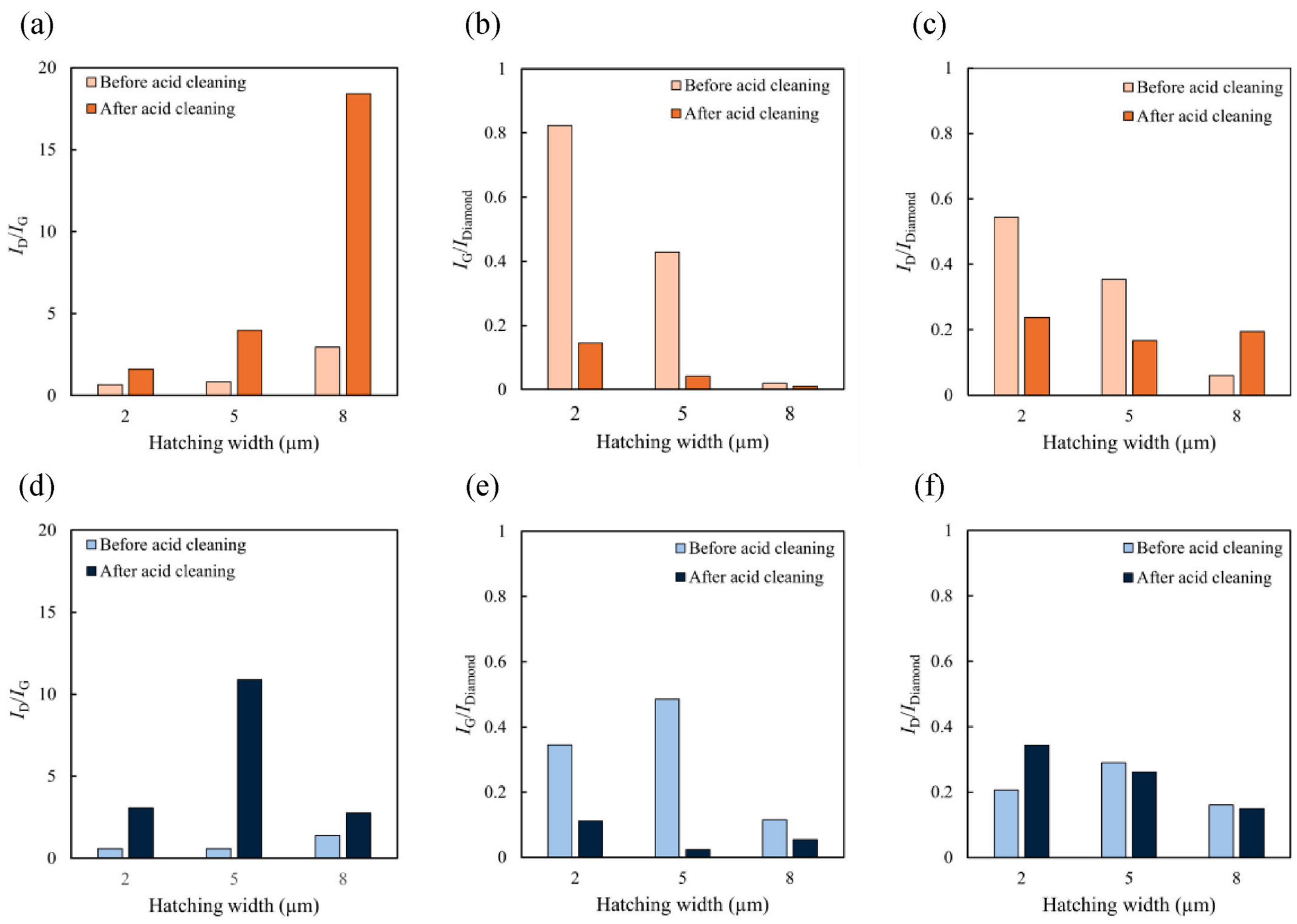

Fig. 13. I_D/I_G, $I_G/I_{Diamond}$, and $I_D/I_{Diamond}$ ratio of the laser irradiated surface at laser fluence of (a)-(c) 2.0 J/cm^2, (d)-(f) 3.5 J/cm^2, at different hatching widths.

graphite structure may increase compared to those before acid cleaning.

3.4. Mechanism of surface formation

Based on the above results, the mechanism of surface formation when laser irradiation is performed on SCD with different hatching widths is discussed as follows. Fig. 14 shows a schematic side view of the irradiated substrate, which represents the changes that occur on the surface of the sample. The hatching width parameter is divided into three cases: (a) wide (50% of the spot diameter or more), (b) intermediate (25 - 50% of the spot diameter), and (c) narrow (25% of the spot diameter or less).

During laser irradiation of SCD, an atmosphere of carbon plasma (carbon vapor) is accumulated above the irradiated surface [29,30]. This carbon vapor is known to remain near the surface for approximately 100 μs [31]. In this study, since the length of each line of hatching irradiation is 300 μm (Fig. 2(b)) and the scanning speed is 50 mm/s, which means the maximum time for a round trip to the same cross-sectional point is 12 ms, the following scan lines will not be irradiated to the existing carbon vapor. This indicates that only the carbon vapor generated by the irradiation of the previous pulse during each line irradiation affects the irradiation surface. Carbon vapor has a heat accumulation effect, causing the surface to reach the graphitization temperature (900 °C), which transforms the surface layer into a graphite layer [32–34]. In this process, LIPSS were formed due to the interference between the surface plasmon and the incident laser light [27]. The thickness of the graphite layer formed and the ratio of nanocrystalline graphite to amorphous carbon differ between the narrow and wide cases of hatching widths. This graphite layer does not grow under laser irradiation; instead, most of this layer is removed by the next pulse and reformed on the newly exposed surface. SCD has high thermal conductivity, so the graphite layer is rapidly cooled immediately after formation. Therefore, that layer tends to form an amorphous structure. When no additional thermal energy is applied or insufficient reheating occurs, the proportion of amorphous carbon becomes high. However, when sufficient thermal energy is applied to this amorphous graphite layer, the carbon atoms rearrange into a more stable layered structure, transforming into nanocrystalline graphite. The heat source in this study is the laser beam wings, the low-intensity tail region of the Gaussian beam profile [35]. The laser beam wings contribute to thermal energy injection without exceeding the ablation threshold. This causes amorphous carbon to turn into nanocrystalline graphite. Therefore, the surface finally observed after irradiation will be either an amorphous carbon formed as a result of rapid cooling or nanocrystalline graphite formed as a result of reheating to the amorphous layer.

In the wide case (Fig. 14(a)), the hatching width exceeds the beam radius, and irradiation occurs at a position distant from the line next to the last line irradiation section. Therefore, the number of times the laser beam wings overlap and irradiate onto the already formed amorphous carbon is quite low. This resulted in fewer reheating cycles to amorphous carbon, reducing the proportion that transformed into nanocrystalline graphite. Consequently, a thin layer with a higher proportion of amorphous carbon was formed (Fig. 14(a) and (d)). As the hatching width approaches 16 μm, the size of the spot diameter, the micro

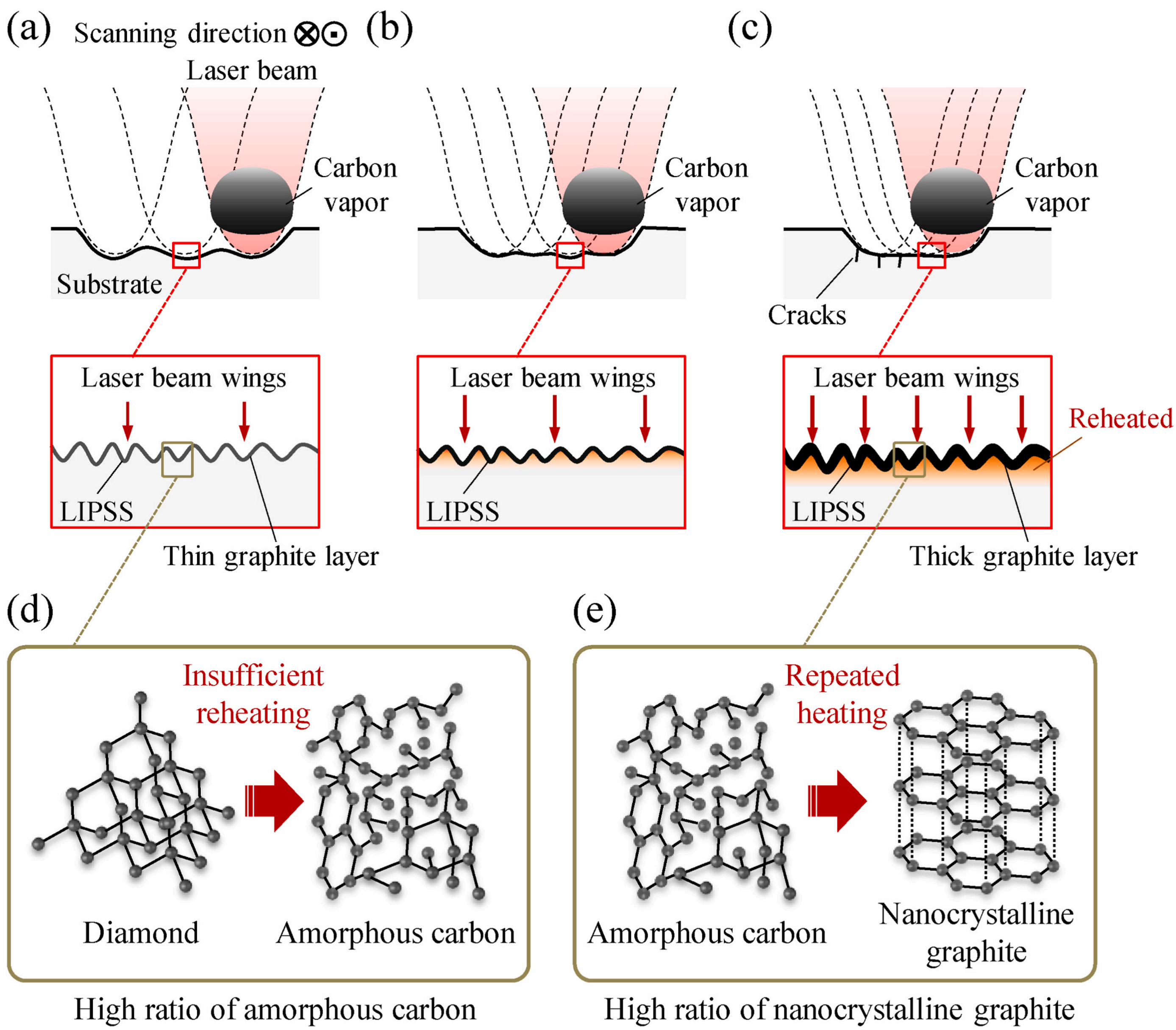

Fig. 14. Schematic images of hatching irradiation of SCD: (a) The wide case of laser scanning hatching width, (b) The intermediate case of laser scanning hatching width, (c) The narrow case of laser scanning hatching width, (d) Change in chemical structure from diamond to amorphous carbon, (e) Change in chemical structure from amorphous carbon to nanocrystalline graphite.

concave shape of the irradiation scar increases due to the material removal mechanism of the laser with a Gaussian energy distribution, as shown in Fig. 8. Therefore, the surface roughness increases as the hatching width is closer to the spot diameter.

On the other hand, in the narrow case (Fig. 14(c)), the hatching width is sufficiently small relative to the laser beam radius, resulting in irradiation at a high overlap rate onto the already formed amorphous carbon. In this case, reheating by the laser beam wings below the ablation threshold becomes dominant. Consequently, repeated additional heating without removal occurs, and thicker, more stable nanocrystalline graphite structures are formed (Fig. 14(c) and (e)). This graphite layer tends to crack and increases the resulting surface roughness. Acid cleaning is needed to reduce the surface roughness by removing the graphite structure from the surface layer.

In the intermediate case (Fig. 14(b)), the surface roughness is smaller than that in the narrow and wide cases. This is because unlike the narrow case, the surface is not cracked; and unlike the wide case, the height of surface waviness caused by the footprint of the Gaussian beam is smaller. In other words, the determining factor for the minimum surface roughness under hatching irradiation is considered to be LIPSS, which were present regardless of whether the hatching width was narrow or wide. However, in the wide case, the undulation caused by the hatching pattern, which was larger than the LIPSS effect, added to the LIPSS irregularities, also increasing overall surface roughness. Thus, it is considered that the SCD surface formation mechanism differs significantly according to the hatching width of the laser.

3.5. Fabrication of micro cavities

Based on the results of hatching irradiation, 300 μm × 300 μm rectangular cavities with flat bottom surfaces and sharp corners were test fabricated in SCD. Fig. 15 shows SEM images of the cavities. Fig. 15 (a) shows a cavity surface machined at the laser fluence of 3.5 J/cm^2, hatching width of 2 μm, where SEM observation was performed before acid cleaning. The irradiated area appears darker than the non-irradiated surface due to its greater depth. A striped pattern appeared

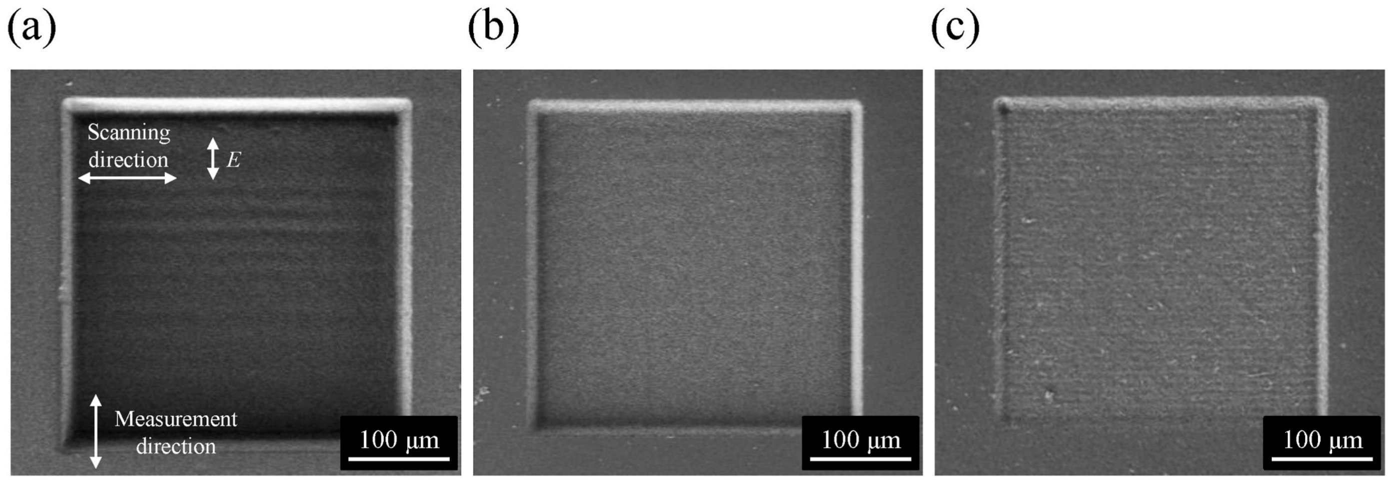

Fig. 15. SEM images of rectangular groove with flat surface (a) before acid cleaning at laser fluence of 3.5 J/cm^2, and hatching width of 2 µm, (b) after acid cleaning at laser fluence of 3.5 J/cm^2, and hatching width of 4 µm, (c) after acid cleaning at laser fluence of 2.0 J/cm^2, and hatching width of 8 µm.

in part of the irradiation area, which may have been caused by temporary instability in the laser intensity due to continuous operation. Fig. 15 (b) shows a cavity machined at a fluence of 3.5 J/cm^2, hatching width of 4 µm, where SEM observation was performed after acid cleaning. The bottom surface was flat without cracks and looks apparently brighter than that shown in Fig. 15(a). In addition, Fig. 15(c) shows a cavity machined at a fluence of 2.0 J/cm^2, hatching width of 8 µm, where SEM observation was performed after acid cleaning. There were lines running parallelly to the scanning direction, with slight periodic irregularities. Fig. 16 shows the cross-sectional profiles for different hatching widths at a laser fluence of 3.5 J/cm^2. The profile of the central region of the irradiated surface was obtained according to the measurement direction shown in Fig. 15(a). As the hatching width decreased, the entire groove bottom surface became flatter. The reason for the sharp decrease in surface roughness at hatching width of 10 µm compared to 16 µm is thought to be due to the diminished influence of the groove shape in the Gaussian energy distribution, which originates the undulation in the hatching pattern. This phenomenon is also confirmed in Fig. 10(b), which shows the surface roughness of the flat surface after acid cleaning.

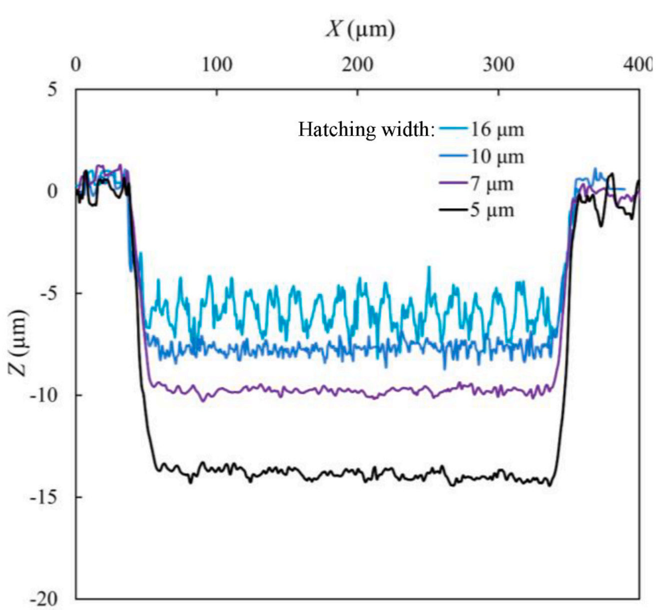

Fig. 16. Cross-sectional profiles after acid cleaning at laser fluence of 3.5 J/cm^2, at different hatching widths.

In addition, the groove depth increased with decreasing hatching width due to the increase in energy per unit area. Such three-dimensional SCD micro features with flat bottom surfaces and sharp corners have been difficult to machine by conventional mechanical processes.

4. Conclusions

In this study, femtosecond pulsed laser irradiation of SCD was carried out to investigate the fundamental micromachining characteristics. The machined surface morphology, roughness, and cross-sectional profiles, as well as material structural changes, were investigated. The following conclusions were obtained.

(1) In line irradiation experiment, at a low scanning speed, microcracks appeared on the machined surface. As the number of scans increased, the cracks expanded to the ablation boundary of the groove. However, by increasing the scanning speed, crack generation was suppressed.
(2) In hatching irradiation experiment, surface roughness decreased with hatching width. Flat surfaces with surface roughness of 0.10 µm Ra were successfully obtained under suitable conditions (hatching width ∼ 10 µm, laser fluence 2.0 ∼ 3.5 J/cm^2, scanning speed 50 mm/s). When the hatching width was too small (2 ∼ 4 µm), however, cracks occurred.
(3) In three-dimensional processing, the laser-machined surfaces were covered with LIPSS at all hatching widths.

Also, the following conclusions were obtained regarding phenomena observed during hatching irradiation.

(4) Raman analysis of the SCD surface after laser irradiation showed that amorphous carbon and nanocrystalline graphite coexisted as a composite material. The surface graphitization depended on the laser fluence and hatching width and was particularly pronounced at low fluence and small hatching width, causing surface roughening.
(5) Acid cleaning removed most of the graphite structure, but a part of the structure remained at the interface with the diamond bulk. Detailed analysis of the Raman peak intensity ratio suggested that the nanocrystalline graphite structure remaining after acid cleaning had defects.
(6) The thickness of the graphite layer and surface roughness depended on the number of reheating cycles due to irradiation of the laser beam wings. At a big hatching width (9 µm or more), a thin layer mainly composed of amorphous carbon was formed

with the high surface roughness. When hatching width was small (2 ∼ 4 μm), a thick layer mainly composed of nanocrystalline graphite was formed, which caused cracks and surface roughening. At an intermediate hatching width (5 ∼ 8 μm), surface roughness was the smallest.

The typical phenomena present in the femtosecond pulsed laser micromachining of SCD were investigated, and the main factors affecting the surface quality and shape profile were identified. The findings of this study provide useful information for the optimization of the laser micromachining process of SCD, which enables creating three-dimensional microstructures for various applications.

CRediT authorship contribution statement

Kodai Koshiishi: Writing – original draft, Visualization, Validation, Methodology, Investigation, Formal analysis, Data curation. **Yuka Yamamuro:** Writing – original draft, Visualization, Methodology, Investigation. **Jiwang Yan:** Writing – review & editing, Supervision, Resources, Project administration, Methodology, Funding acquisition, Conceptualization.

Data availability statement

No data, models, or code were generated or used for this paper.

Declaration of competing interest

The authors declare that they have no known competing financial interests or personal relationships that could have appeared to influence the work reported in this paper.

Acknowledgements

This work has been partially supported by Japan Society for the Promotion of Science under the Grant-in-Aid for Scientific Research (A), project number 25H00709.

References

[1] Zong WJ, Cheng K, Li D, Sun T, Liang YC. The ultimate sharpness of single-crystal diamond cutting tools—Part I: theoretical analyses and predictions. Int J Mach Tool Manufact Apr. 2007;47(5):852–63. https://doi.org/10.1016/J.IJMACHTOOLS.2006.04.001.
[2] Forsberg P, Karlsson M. High aspect ratio optical gratings in diamond. Diam Relat Mater Apr. 2013;34:19–24. https://doi.org/10.1016/j.diamond.2013.01.009.
[3] Wort CJH, Balmer RS. Diamond as an electronic material. Mater Today Jan. 2008;11(1–2):22–8. https://doi.org/10.1016/S1369-7021(07)70349-8.
[4] Zhang Z, Gu K, Chen G, Imura M, Liao M. Electrical actuation of single-crystal diamond MEMS resonators at high temperatures. Function Diamond Dec. 2024;4(1):2346085. https://doi.org/10.1080/26941112.2024.2346085.
[5] Wang X, Fang S, Nishimura K, Jiang N, Yi J, Yu L. Rapid smoothing of diamond surfaces. Mater Lett Dec. 2025;400:139126. https://doi.org/10.1016/j.matlet.2025.139126.
[6] Mathis A, et al. Micromachining along a curve: femtosecond laser micromachining of curved profiles in diamond and silicon using accelerating beams. Appl Phys Lett Aug. 2012;101(7):071110. https://doi.org/10.1063/1.4745925.
[7] Kononenko TV, et al. Femtosecond laser microstructuring in the bulk of diamond. Diam Relat Mater Feb. 2009;18(2–3):196–9. https://doi.org/10.1016/j.diamond.2008.07.014.
[8] Odake S, Ohfuji H, Okuchi T, Kagi H, Sumiya H, Irifune T. Pulsed laser processing of nano-polycrystalline diamond: a comparative study with single crystal diamond. Diam Relat Mater May 2009;18(5–8):877–80. https://doi.org/10.1016/j.diamond.2008.10.066.
[9] Takayama N, Yan J. Mechanisms of micro-groove formation on single-crystal diamond by a nanosecond pulsed laser. J Mater Process Technol May 2017;243:299–311. https://doi.org/10.1016/j.jmatprotec.2016.12.032.
[10] Takayama N, Ishizuka J, Yan J. Microgrooving of a single-crystal diamond tool using a picosecond pulsed laser and some cutting tests. Precis Eng Jul. 2018;53:252–62. https://doi.org/10.1016/j.precisioneng.2018.04.009.
[11] Okamoto Y, Okubo T, Kajitani A, Okada A. High-quality micro-shape fabrication of monocrystalline diamond by nanosecond pulsed laser and acid cleaning. Int J Extrem Manuf Jun. 2022;4(2):025301. https://doi.org/10.1088/2631-7990/ac5a6a.
[12] Ramanathan D, Molian PA. Micro- and sub-micromachining of type IIa single crystal diamond using a ti:sapphire femtosecond laser. J Manuf Sci Eng May 2002;124(2):389–96. https://doi.org/10.1115/1.1459083.
[13] Wang CZ, Ho KM, Shirk MD, Molian PA. Laser-induced graphitization on a diamond (111) surface. Phys Rev Lett Nov. 2000;85(19):4092–5. https://doi.org/10.1103/PhysRevLett.85.4092.
[14] Wu M, Guo B, Zhao Q, He P, Zeng Z, Zang J. The influence of the ionization regime on femtosecond laser beam machining mono-crystalline diamond. Opt Laser Technol Oct. 2018;106:34–9. https://doi.org/10.1016/j.optlastec.2018.03.031.
[15] Granados E, Martinez-Calderon M, Gomez M, Rodriguez A, Olaizola SM. Photonic structures in diamond based on femtosecond UV laser induced periodic surface structuring (LIPSS). Opt Express Jun. 2017;25(13):15330. https://doi.org/10.1364/OE.25.015330.
[16] Banik S, Indhu R, Arunachalam N, Rao MSR. Femtosecond laser-induced surface structuring for improved surface characteristics of single crystal diamond. Diam Relat Mater Apr. 2025;154:112240. https://doi.org/10.1016/j.diamond.2025.112240.
[17] Watanabe K, Toida Y. Determination of boron in graphite by a wet oxidation decomposition/curcumin photometric method. Bunseki Kagaku (Jpn Anal) 1995;44(11):939–42. https://doi.org/10.2116/bunsekikagaku.44.939 (in Japanese).
[18] Imoto Y, Yan J. Thermochemical micro imprinting of single-crystal diamond surface using a nickel mold under high-pressure conditions. Appl Surf Sci May 2017;404:318–25. https://doi.org/10.1016/j.apsusc.2017.01.303.
[19] Pichot V, et al. An efficient purification method for detonation nanodiamonds. Diam Relat Mater Jan. 2008;17(1):13–22. https://doi.org/10.1016/j.diamond.2007.09.011.
[20] Taylor LL, Qiao J, Qiao J. Optimization of femtosecond laser processing of silicon via numerical modeling. Opt Mater Express Sep. 2016;6(9):2745. https://doi.org/10.1364/OME.6.002745.
[21] Yamamuro Y, Shimoyama T, Yan J. 'Microscale Surface Patterning of Zirconia by Femtosecond Pulsed Laser Irradiation,'. Int J Precision Eng Manufact Green Technol Mar. 2022;9(2):619–32. https://doi.org/10.1007/s40684-021-00362-3.
[22] Ohmagari S, Yamada H, Umezawa H, Chayahara A, Teraji T, Shikata S. Characterization of free-standing single-crystal diamond prepared by hot-filament chemical vapor deposition. Diam Relat Mater Sep. 2014;48:19–23. https://doi.org/10.1016/j.diamond.2014.06.001.
[23] Knight DS, White WB. Characterization of diamond films by Raman spectroscopy. J Mater Res Apr. 1989;4(2):385–93. https://doi.org/10.1557/JMR.1989.0385.
[24] Chu PK, Li L. Characterization of amorphous and nanocrystalline carbon films. Mater Chem Phys Apr. 2006;96(2–3):253–77. https://doi.org/10.1016/j.matchemphys.2005.07.048.
[25] Rehman ZU, Janulewicz KA. Structural transformation of monocrystalline diamond driven by ultrashort laser pulses. Diam Relat Mater Nov. 2016;70:194–200. https://doi.org/10.1016/j.diamond.2016.11.004.
[26] Kononenko VV, et al. Highly oriented graphite produced by femtosecond laser on diamond. Appl Phys Lett Jun. 2019;114(25). https://doi.org/10.1063/1.5097986.
[27] Sartori AF, et al. Laser-induced periodic surface structures (LIPSS) on heavily boron-doped diamond for electrode applications. ACS Appl Mater Interfaces Dec. 2018;10(49):43236–51. https://doi.org/10.1021/acsami.8b15951.
[28] Cobb SJ, et al. Assessment of acid and thermal oxidation treatments for removing sp2 bonded carbon from the surface of boron doped diamond. Carbon N Y Oct. 2020;167:1–10. https://doi.org/10.1016/j.carbon.2020.04.095.
[29] Han H, He M, Liu H, Zhang B, Zhou C. Damage evolution and crystalline orientation effects in ultrafast laser micro/nano processing of single-crystal diamond. Opt Laser Technol Feb. 2024;169:110120. https://doi.org/10.1016/j.optlastec.2023.110120.
[30] Kononenko VV, et al. Highly oriented graphite produced by femtosecond laser on diamond. Appl Phys Lett Jun. 2019;114(25):251903. https://doi.org/10.1063/1.5097986.
[31] Yousfi H, Abdelli-Messaci S, Ouamerali O, Dekhira A. Atomic and molecular species Post-2 μs dynamics in laser-induced carbon plasmas in air. Appl Spectrosc Mar. 2021;75(3):287–98. https://doi.org/10.1177/0003702820971602.
[32] Seal M. The effect of surface orientation on the graphitization of diamond. Physica Status Solidi (b) Jan. 1963;3(4):658–64. https://doi.org/10.1002/pssb.19630030408.
[33] Evans T, James PF. A study of the transformation of diamond to graphite. Proc R Soc Lond A Math Phys Sci Jan. 1964;277(1369):260–9. https://doi.org/10.1098/rspa.1964.0020.
[34] Davies G, Evans T. Graphitization of diamond at zero pressure and at a high pressure. Proceed Royal Soc London A Math Phys Sci Jun. 1972;328(1574):413–27. https://doi.org/10.1098/rspa.1972.0086.
[35] Zuffi AVF, Ricardo dos Santos J, Maldonado EP, Vieira ND, Samad RE. Femtosecond laser-plasma dynamics study by a time-resolved Mach–Zehnder-like interferometer. Appl Opt Mar. 2023;62(8):C128. https://doi.org/10.1364/ao.477395.